Inorganic Chemistry

Regulating Bimetallic Asymmetry of $Mn^{2+}-O-Fe^{3+}$ Domain in Layered Double Hydroxides for Lattice Oxygen Activation toward Enhanced Photocatalytic Toluene Oxidation

Haohong Liao,[#] Jingfang Sun,[#] Xiuwen Wang, Qing Tong, Tao Liu,* Weixin Zou,* and Lin Dong

Cite This: *Inorg. Chem.* 2025, 64, 17448−17458

Read Online

ACCESS | Metrics & More | Article Recommendations | Supporting Information

ABSTRACT: In photocatalytic toluene oxidation, traditional semiconductor catalysts still face the problem of insufficient generation of reactive oxygen species (ROS). Herein, we first regulate the bimetallic asymmetry in layered double hydroxide (LDH) photocatalysts via different metal electronegativities to activate lattice oxygen for ROS generation. The MnFe-LDH, MnAl-LDH, and ZnFe-LDH photocatalysts with various electronegativities (Mn: 1.55, Al: 1.61, Zn: 1.65, Fe: 1.83) were designed, and MnFe-LDH with the maximum electronegativity difference achieved the best toluene oxidation. Characterizations and calculations revealed that due to the enhanced bimetallic asymmetry of $Mn^{2+}-O-Fe^{3+}$ domain, the significant contraction and expansion of Mn−O and Fe−O bonds occurred, respectively, leading to enhanced lattice oxygen activation and oxygen vacancy generation, and an intensive built-in electric field caused by charge transfer from Mn to Fe in MnFe-LDH, both of which, under light irradiation, promoted O_2 adsorption on *in situ*-formed oxygen vacancy along with photoelectrons, leading to ROS formation. Specifically, the hydroxyl groups linking bimetallic sites in MnFe-LDH were beneficial for methyl oxidation and the subsequent ring-opening of toluene. This study provides fresh insights into the design of LDH-based photocatalysts for toluene oxidation.

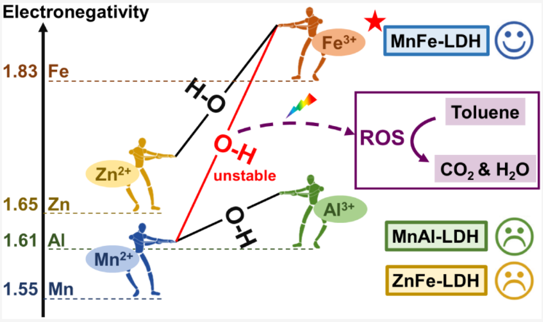

1. INTRODUCTION

Volatile organic compounds (VOCs) are a class of pollutants widely present in both indoor and outdoor environments.[1] Among them, toluene, as a typical aromatic hydrocarbon, poses a serious threat to human health and indoor air quality due to its toxicity and tendency to accumulate in indoor environments.[2] Toluene not only exerts toxic effects on the central nervous system through respiratory exposure but may also trigger allergic reactions and respiratory system diseases.[3] In recent years, the photocatalytic oxidation technology has emerged as a green and highly efficient method for pollution control, particularly demonstrating significant advantages in the removal of VOCs.[4−6] This technology utilizes electron−hole pairs generated by semiconductor materials under light irradiation to effectively oxidize and decompose organic pollutants like toluene into harmless products, such as carbon dioxide and water.[7−9] Compared to traditional methods of adsorption[10] and combustion,[11] the photocatalytic oxidation offers several advantages, including low energy consumption, mild reaction conditions, and ease of operation, making it particularly suitable for indoor air purification.[12,13]

Despite its advantages, the photocatalytic oxidation technology still faces critical challenges, such as rapid recombination and slow transport of photogenerated electron−hole pairs,[14−16] which limit the diversity and quantity of reactive oxygen species (ROS) generated during reactions. Hydroxyl radicals (•OH), as a type of ROS, play a crucial role in accelerating the oxidation and ring-opening mineralization of toluene.[17−19] Recently, layered double hydroxides (LDHs), as hydroxyl-rich materials, are gaining increasing attention in photocatalysis research.[20,21] These materials are more likely to generate hydroxyl radicals under light irradiation, which accelerate the oxidation of toluene.[22] Besides, their unique layered structure effectively reduces the level of recombination of photogenerated electron−hole pairs and provides abundant active sites for toluene adsorption and activation. For example, Liu et al.[12] prepared ZnSn LDH photocatalyst with electron-rich hydroxyl groups for the degradation of VOCs. The electron-rich hydroxyl groups in ZnSn LDH enhance the interaction between aromatic VOCs and the photocatalyst and promote the generation of ROS, thereby achieving rapid ring opening and deep oxidation of aromatic rings. In addition, compared with traditional catalysts, LDHs exhibit larger

Received: June 19, 2025
Revised: August 10, 2025
Accepted: August 13, 2025
Published: August 21, 2025

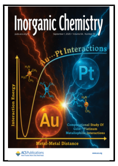

Downloaded via NANJING UNIV on September 23, 2025 at 02:57:23 (UTC).
See https://pubs.acs.org/sharingguidelines for options on how to legitimately share published articles.

© 2025 American Chemical Society

https://doi.org/10.1021/acs.inorgchem.5c02813

specific surface areas, offering more adsorption sites for the reactants. Moreover, their catalytic performance can be optimized by adjusting the ratios and types of metal ions.[23]

In the reactions of catalytic oxidation, the activated lattice oxygen plays an important role in the conversion of reactant molecules, as well as improving the oxidation capacity for deep mineralization,[24] which commonly refers to the Mars-van Krevelen mechanism. Besides, the synergistic effect between the bimetallic components contributes to the enhancement of catalytic activity.[25,26] For example, Zhu et al.[27] fabricated CuO-Fe_3O_4 composites with the active sites of Cu^{2+}−O−Fe^{3+}, leading to the activation of surface lattice oxygen, thereby enhancing the catalytic degradation of VOCs. Chen et al.[24] fabricated $Sr_2Sb_2O_7$ with high lattice oxygen activity, which can significantly accelerate the generation of ROS and achieve the stable photocatalytic mineralization of toluene. Therefore, the asymmetry between the two metal ions significantly impacts oxygen reactivity, and specifically, stronger asymmetry facilitates better oxygen activation.[28] Actually, LDHs have accurate structures with adjustable metal ions, which are helpful for regulating bimetallic asymmetry to activate lattice oxygen. However, the relationships between LDHs with bimetallic asymmetry and toluene oxidation are unclear, and the regulation mechanism of lattice oxygen activation in LDH photocatalysts to enhance oxidation performance is worth studying.

Herein, considering the lattice oxygen activation closely related to metal−oxygen bond energy, which could be affected by the electronegativity difference of metal ions in LDHs, the MnFe-LDH, MnAl-LDH, and ZnFe-LDH photocatalysts with different electronegativities (Mn: 1.55, Al: 1.61, Zn: 1.65, Fe: 1.83) have been synthesized for the enhanced photocatalytic toluene oxidation (Figure 1). The results of XANES, *in situ* XPS, *in situ* EPR, and DFT calculations show the significant stretching of metal−oxygen bonds in MnFe-LDH, owing to the largest electronegativity difference between Mn and Fe with the strongest metal asymmetry, compared with MnAl-LDH and ZnFe-LDH. Therefore, MnFe-LDH exhibits enhanced oxygen activation and faster photogenerated charge transfer under the intensive built-in electric field of Mn^{2+}−O−Fe^{3+} domain, which promotes ROS generation. Furthermore, the photocatalytic processes of toluene oxidation are explored by *in situ* DRIFTS and calculations. This work aims to elucidate the structure−activity relationship between bimetallic asymmetry and the oxidation performance of LDH photocatalysts, providing new insights for the design of highly efficient photocatalysts for VOC degradation.

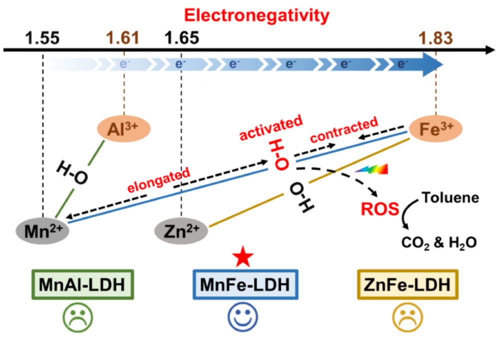

Figure 1. Regulation of LDHs with bimetallic asymmetry by different electronegativities for the enhanced photocatalytic oxidation of toluene.

2. METHODS

2.1. Synthesis of Photocatalysts. MnFe-LDH, MnAl-LDH, and ZnFe-LDH samples were successfully synthesized via a hydrothermal method[29] as follows. Taking MnFe-LDH as an example, 15 mmol of $Mn(NO_3)_2 \cdot 4H_2O$, 5 mmol of $Fe(NO_3)_3 \cdot 9H_2O$, and 30 mmol of urea were added into 60 mL of dimethylformamide (DMF) solution and stirred at room temperature for 30 min. The mixture was then collected in a Teflon-lined stainless steel autoclave, sealed, and maintained at 120 °C for 24 h, followed by cooling to room temperature. Subsequently, the precipitate was collected, washed several times with deionized water and ethanol, and then dried overnight at 60 °C. The preparation of MnAl-LDH followed the same procedure as for MnFe-LDH, except that $Fe(NO_3)_3 \cdot 9H_2O$ was replaced with an equimolar amount of $Al(NO_3)_3 \cdot 9H_2O$. Similarly, ZnFe-LDH was prepared using the same method as MnFe-LDH, but with $Mn(NO_3)_2 \cdot 4H_2O$ being replaced by an equimolar amount of $Zn(NO_3)_2 \cdot 6H_2O$. The successful synthesis of the three photocatalysts was verified by the characterization results of XRD and FT-IR (see details in Figures S1 and S2).

2.2. Characterizations. Details of the characterizations of X-ray diffraction (XRD), Fourier-transform infrared spectroscopy (FT-IR), UV−vis diffuse reflectance spectroscopy (UV−vis DRS), X-ray photoelectron spectroscopy (XPS), X-ray absorption near edge spectroscopy (XANES), extended X-ray absorption fine structure (EXAFS), transient photocurrent response, electrochemical impedance spectroscopy (EIS), Mott−Schottky curve, electron paramagnetic resonance (EPR), and *in situ* diffuse reflectance infrared Fourier-transform spectroscopy (*in situ* DRIFTS) are available in the Supporting Information.

2.3. Photocatalytic Toluene Oxidation. The photocatalytic oxidation of toluene was conducted in a 1.5 L cylindrical reactor using a 300 W xenon lamp as the light source. Catalyst powder (100 mg) was uniformly distributed on a 304-mm-thick stainless steel mesh. The reaction gas of toluene (50 $mL \cdot min^{-1}$) was maintained at a concentration of 20 ppm by a balance of high-purity air (21% O_2, balanced with N_2), which was continuously vented into the reactor at a specific relative humidity value (RH = 65%), which was controlled by the ratio of water vapor and air during the reaction process and flowed through the stainless steel mesh lined with the catalyst and then into the gas chromatography column for detection. The photoreaction was initiated by adsorption for 40 min in the dark, followed by photocatalytic toluene oxidation under 300 W xenon lamp irradiation, and the reaction product was analyzed by chromatography. The toluene conversion and mineralization were calculated as follows:

$$C_7H_8 \text{ conversion (\%)} = \frac{[C_7H_8]_{in} - [C_7H_8]_{out}}{[C_7H_8]_{in}} \times 100\%$$

$$C_7H_8 \text{ mineralization (\%)} = \frac{[CO_2]_{out}}{7 \times ([C_7H_8]_{in} - [C_7H_8]_{out})} \times 100\%$$

where $[C_7H_8]_{in}$ and $[C_7H_8]_{out}$ represent the inlet and outlet concentrations (ppm) of gas-phase toluene, respectively, and

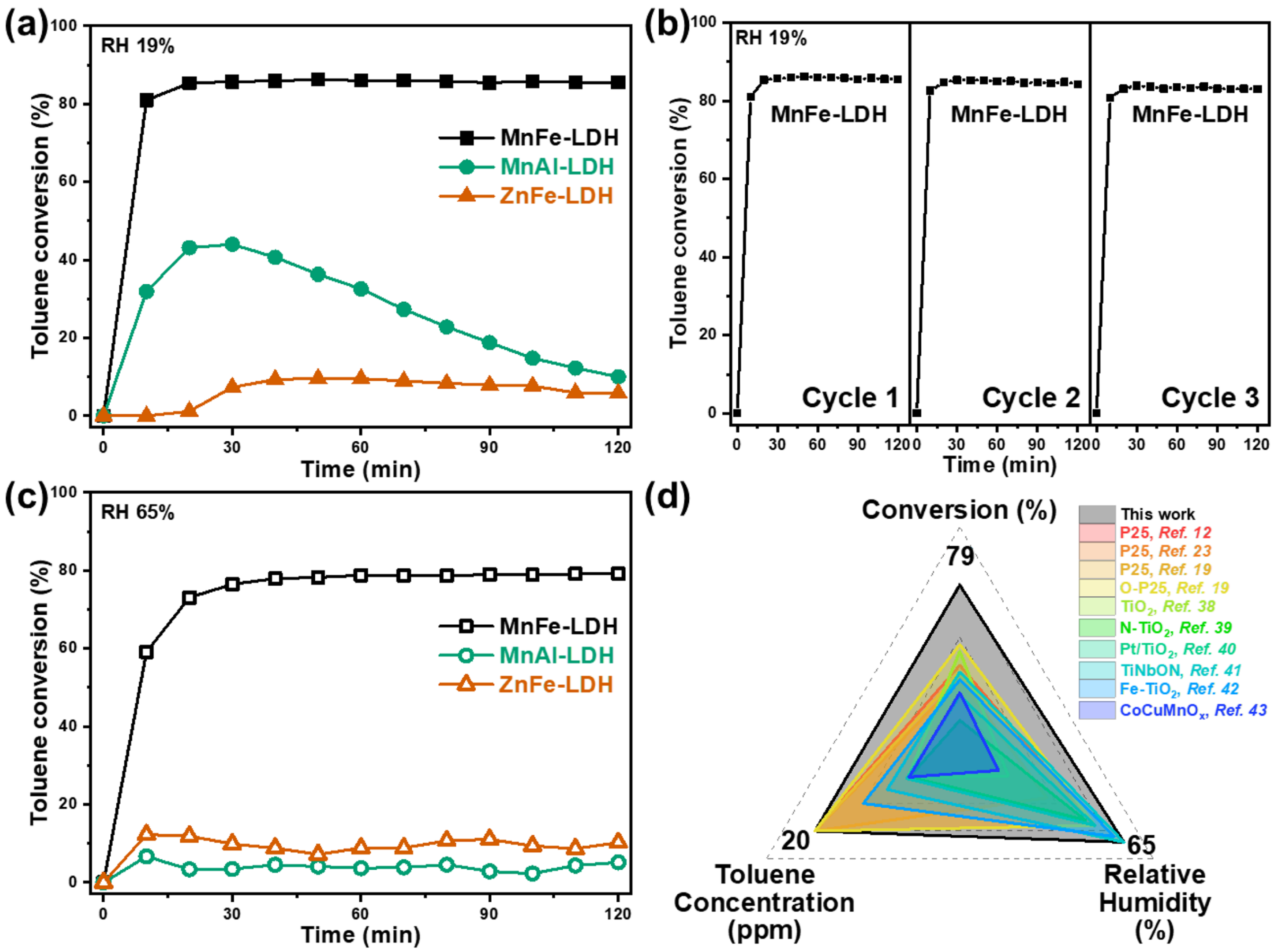

Figure 2. (a) Photocatalytic activities of toluene oxidation of the samples and (b) cycle test over MnFe-LDH with RH = 19%. (c) Photocatalytic activities of toluene oxidation with RH = 65% and (d) the performance comparison of photocatalytic toluene oxidation with that found in the literature.[12,19,23,38−43]

$[CO_2]_{out}$ represents the outlet concentrations (ppm) of gas-phase carbon dioxide.

2.4. Details of Density Functional Theory (DFT) Calculations. We used the Vienna Ab Initio Package (VASP)[30,31] to conduct spin-polarized DFT calculations in the generalized gradient approximation (GGA) using the PBE[32] formulation. For the ionic cores, we opted for projected augmented wave (PAW) potentials[33,34] and accounted for valence electrons using a plane wave basis set with a kinetic energy cutoff of 400 eV. Partial occupancies of the Kohn−Sham orbitals were permitted using the Gaussian smearing method and a width of 0.05 eV. The electronic energy was deemed self-consistent if the energy change was less than 10^{-5} eV. A geometry optimization was considered converged if the force change was less than 0.02 eV/Å. To describe the dispersion interactions, Grimme's DFT-D3 methodology was utilized.[35] The atomic charges were obtained through Bader's analysis[36] using the numerical implementation developed by Henkelman et al.[37] The adsorption energy (E_{ads}) of adsorbate A was calculated as follows:

$$E_{ads} = E_{A/Surf} - E_{Surf} - E_{A(g)}$$

where $E_{A/Surf}$, E_{Surf}, and $E_{A(g)}$ represented the energies of the adsorbate A on the surface, the clean surface, and the isolated A molecule, respectively. The energy of the isolated A molecule was calculated in a cubic periodic box with a side length of 20 Å, using a 1 × 1 × 1 Monkhorst−Pack k-point grid for Brillouin zone sampling.

3. RESULTS AND DISCUSSION

3.1. Photocatalytic Performance of Toluene Oxidation. The photocatalytic performance of toluene oxidation on MnFe-LDH, MnAl-LDH, and ZnFe-LDH samples was carried out under light irradiation with a full spectrum. As shown in Figures 2a and S3, MnFe-LDH exhibits the best toluene oxidation activity, achieving a degradation efficiency of 86% and a mineralization rate of 89%, whereas MnAl-LDH and ZnFe-LDH exhibit poorer toluene oxidation activities. In addition, the toluene degradation rates of MnAl-LDH and ZnFe-LDH at 120 min show a noticeable decrease compared to their maximum values, indicating their rapid deactivation. Moreover, MnFe-LDH shows excellent stability over three cycles of testing (Figure 2b), maintaining a degradation rate of toluene above 80%. Furthermore, we also determined the photocatalytic performance of toluene oxidation under reaction conditions with the relative humidity (RH) of 65%. MnFe-LDH still exhibits excellent water resistance performance (Figures 2c and S4b) and maintains excellent stability

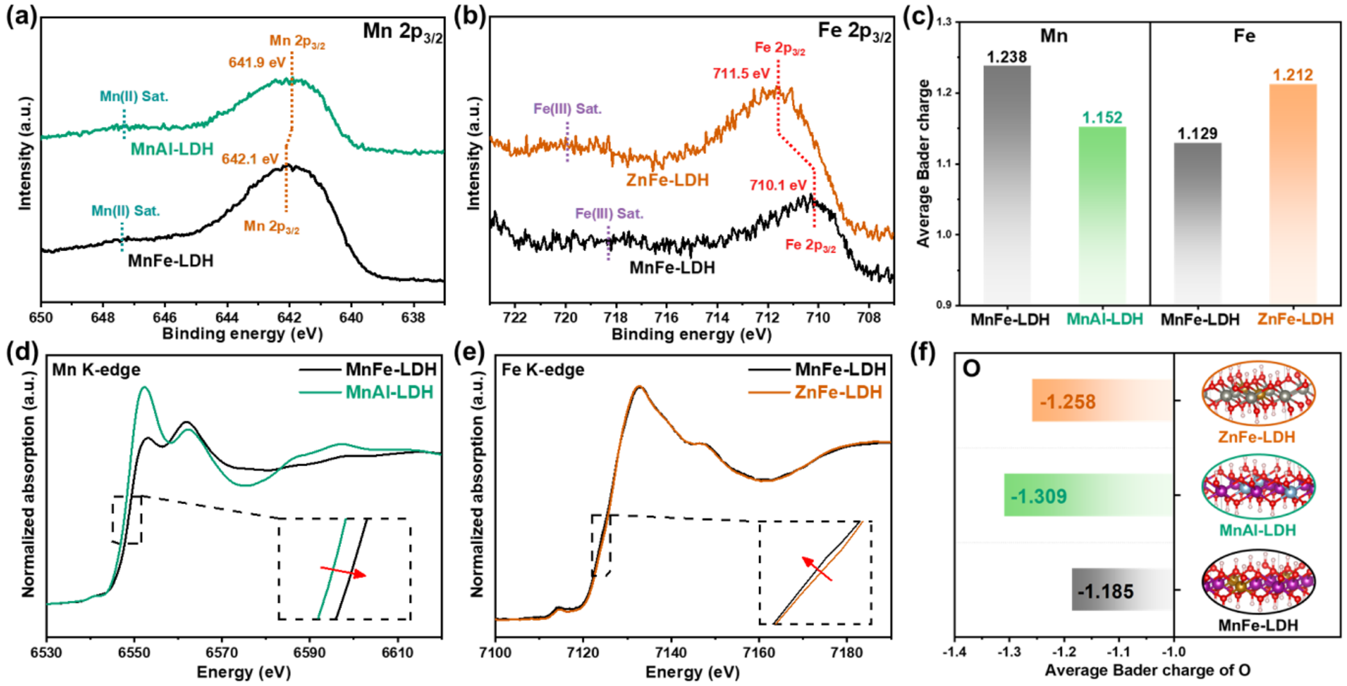

Figure 3. XPS spectra of (a) Mn $2p_{3/2}$ for MnFe-LDH and MnAl-LDH and (b) Fe $2p_{3/2}$ for MnFe-LDH and ZnFe-LDH. (c) The average Bader charges of Mn and Fe. The normalized (d) Mn and (e) Fe K-edge XANES spectra. (f) The average Bader charges of oxygen in the photocatalysts.

(Figure S4a), whereas the performance of MnAl-LDH and ZnFe-LDH are worse. Furthermore, the photocatalytic performance of toluene oxidation over MnFe-LDH under visible light (Figure S5) indicates that MnFe-LDH possesses both excellent visible light utilization and good stability. Compared with other reported literature[12,19,23,38−43] (Figure 2d), it is demonstrated that the MnFe-LDH photocatalyst has better performance in toluene oxidation. To further explore the excellent photocatalytic performance of MnFe-LDH, in comparison with MnAl-LDH and ZnFe-LDH, we conducted the following detailed characterizations and calculations.

3.2. Bimetallic Asymmetry Differences. For toluene oxidation, the activation ability of the lattice oxygen-linking bimetallic sites is of significance, which could be affected by the bimetallic asymmetry in the photocatalyst. Due to the differences in the electronegativities (Mn: 1.55, Al: 1.61, Zn: 1.65, Fe: 1.83) of the divalent and trivalent metal ions constituting MnFe-LDH, MnAl-LDH, and ZnFe-LDH, the valence state changes and charge distribution differences in the bimetallic sites of the photocatalysts are analyzed by XPS, XAFS, and DFT calculations.

In the XPS spectra (Figure S6), it is shown that Mn and Zn ions mainly exist in the divalent form, while Fe and Al ions are primarily in the trivalent state. Notably, in the XPS spectra of Mn $2p_{3/2}$ (Figure 3a), the binding energy of Mn species in MnFe-LDH is shifted to a higher value compared with MnAl-LDH, which suggests that electrons on Mn^{2+} in MnFe-LDH are lost. In addition, the XPS spectra of Fe $2p_{3/2}$ are also determined. In Figure 3b, compared with ZnFe-LDH, the binding energy of Fe species in MnFe-LDH is shifted to a lower value, indicating that electrons are accumulated on Fe^{3+} in MnFe-LDH. Based on the above XPS results, it is suggested that a stronger charge transfer[44] is present in the Mn^{2+}−O−Fe^{3+} domain of MnFe-LDH, indicating its greatest bimetallic asymmetry difference.

The Bader charges of atoms in the photocatalysts can also demonstrate the gain or loss of electrons as well as the charge distribution at an atomic level,[45,46] which is beneficial for demonstrating bimetallic asymmetry differences. The Bader charges of Mn and Fe atoms in MnFe-LDH, MnAl-LDH, and ZnFe-LDH are calculated through DFT computations, respectively. In Figure 3c, the average Bader charge value of Mn atoms in MnFe-LDH is higher than that of MnAl-LDH, whereas the value of Fe atoms in MnFe-LDH is lower than that of ZnFe-LDH. Therefore, there are more electrons lost on Mn atoms and accumulated on Fe atoms in the MnFe-LDH, consistent with the XPS results, further confirming that the Mn^{2+}−O−Fe^{3+} domain in MnFe-LDH with the strongest charge transfer exhibits the most obvious bimetallic asymmetry due to the differences in the metal electronegativities.

Moreover, the XAFS spectra are used to investigate the changes in the valence states of the metal ions in MnFe-LDH, MnAl-LDH, and ZnFe-LDH. In the Mn K-edge XANES spectra (Figure 3d), compared with MnAl-LDH, the absorption edge energy of Mn^{2+} in MnFe-LDH is shifted to higher energy, indicating a higher average valence state of Mn^{2+} in MnFe-LDH.[47] In addition, the Fe K-edge XANES spectra (Figure 3e) showed that the absorption edge energy of Fe^{3+} in MnFe-LDH is lower than that of ZnFe-LDH, indicating that the Fe^{3+} in MnFe-LDH has a lower average valence state.[48] On the basis of the Mn and Fe K-edge XANES spectra, combined with the results of XPS and Bader charges, it is suggested that there is a more obvious charge transfer in the Mn^{2+}−O−Fe^{3+} domain of MnFe-LDH due to its greater difference in bimetallic asymmetry, resulting from the different metal electronegativities.

3.3. Lattice Oxygen Activation and ROS Generation. Generally, the bimetallic asymmetry would have an important role in the lattice oxygen activation, as determined by EXAFS spectra, DFT calculation, *in situ* XPS, and *in situ* EPR characterizations. The changes in Mn−O and Fe−O bond

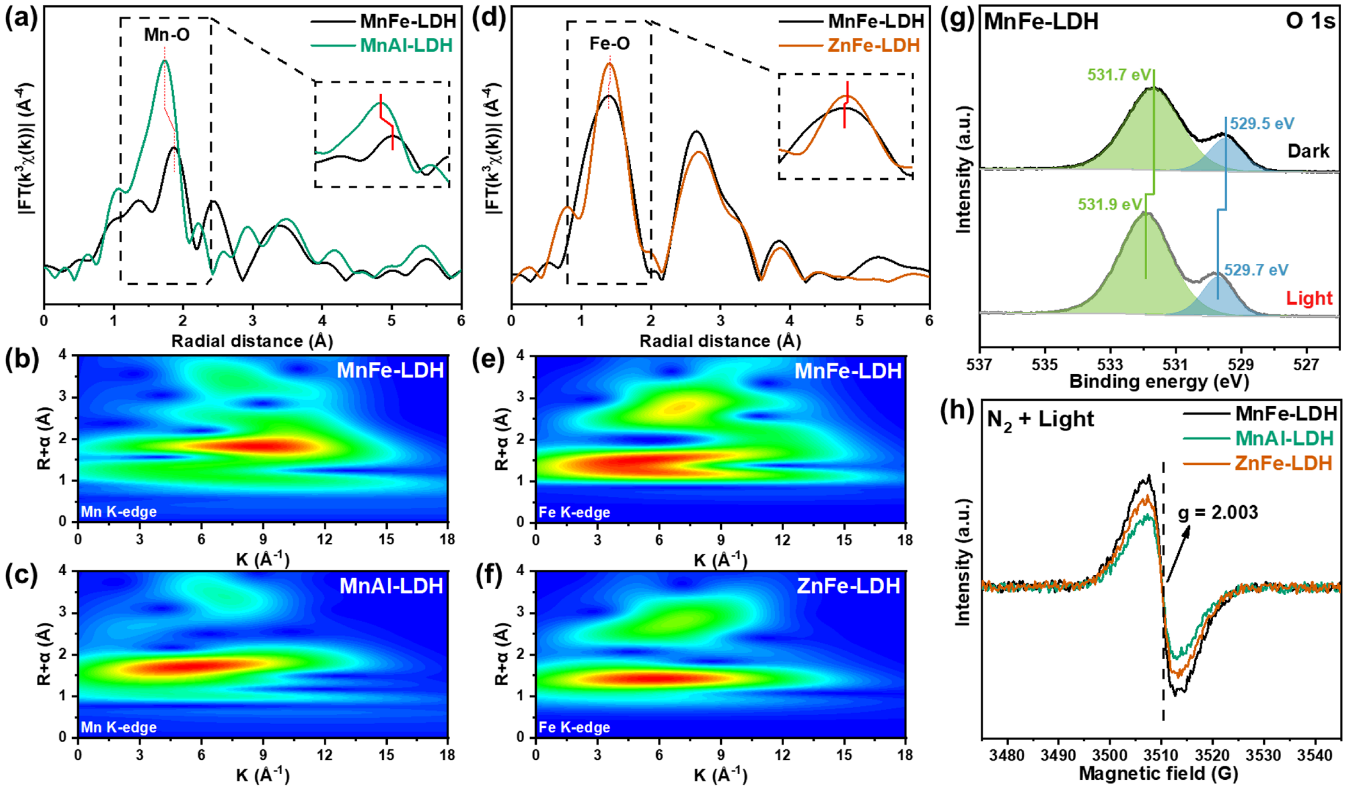

Figure 4. Fourier transform and Morlet wavelet transform results of the (a−c) Mn and (d−f) Fe K-edge EXAFS. (g) XPS spectra of O 1s for MnFe-LDH under dark or light condition. (h) *In situ* EPR spectra collected in a flow of N_2 under light conditions.

lengths are analyzed using EXAFS spectra to study the metal−oxygen bond. In Figure 4a−f, the EXAFS results of Mn and Fe K-edge show that the Mn−O bond length in MnFe-LDH shifts to a higher value compared to that in MnAl-LDH, while the Fe−O bond length in MnFe-LDH shifts to a lower value compared to that in ZnFe-LDH, which suggest that the Mn−O bond expansion and Fe−O bond contraction are obvious in MnFe-LDH.[49,50] In addition, the average Bader charges of oxygen atoms in MnFe-LDH, MnAl-LDH, and ZnFe-LDH were investigated (Figure 3f), revealing that the average Bader charge of oxygen atoms in the MnFe-LDH (−1.185) has the most obvious change compared to f MnAl-LDH (−1.309) and ZnFe-LDH (−1.258), which indicates that the greatest difference in bimetallic asymmetry in MnFe-LDH leads to the highest activity of lattice oxygen.

Moreover, *in situ* XPS spectra of the O 1s under dark or light conditions are carried out. In Figure 4g, it is observed that under illumination, the peaks of oxygen species in the MnFe-LDH photocatalyst shift toward higher binding energies, suggesting a decreased electron density of oxygen, which indicates easier activation of lattice oxygen in MnFe-LDH under light,[47,51] consistent with the Bader charges. However, in MnAl-LDH and ZnFe-LDH (Figure S7), the peaks of all oxygen species have no obvious shift under the conditions of dark and illumination, indicating that their activation of lattice oxygen is more difficult than that of MnFe-LDH. To further confirm the ease of lattice oxygen activation in MnFe-LDH, *in situ* EPR was used to characterize the oxygen vacancy (Ov) formation under light and N_2 conditions. As shown in Figure 4h, the signal at $g = 2.003$ is attributed to Ov,[52] suggesting that the MnFe-LDH sample surface has more Ov than the other two under illumination, which further confirms that the activation of lattice oxygen in MnFe-LDH is more likely to occur, consistent with the *in situ* XPS results of O 1s under light.

Furthermore, *in situ* XPS of Mn 2p and Fe 2p in dark and light conditions has suggested that the Mn^{2+}−O−Fe^{3+} domain of MnFe-LDH could play a role in the formation of built-in electric field for the enhanced photogenerated charge transfer. In Figure 5a,b, once the light is introduced, the valence states of Mn and Fe decrease and increase, respectively, which indicates that the photogenerated electrons on Mn^{2+} and holes on Fe^{3+} are present in MnFe-LDH,[53,54] consistent with the direction of built-in electric field, which results from the bimetallic asymmetry of Mn^{2+}−O−Fe^{3+} domain in MnFe-LDH, leading to the efficient separation and migration of photogenerated carriers. Besides, UV−vis DRS results (Figure S8) showed that MnFe-LDH exhibits the widest absorption range, with stronger absorption in the visible light region compared to MnAl-LDH and ZnFe-LDH. This indicates that MnFe-LDH has a stronger light absorption capacity, which is beneficial for efficient light utilization and the generation of photogenerated charge carriers. Based on the results of Mott−Schottky curves and XPS VB in Figure S9, the band structures of the three samples showed that MnAl-LDH has a wider bandgap, which is not conducive to the transition of photogenerated carriers. Whereas ZnFe-LDH has a narrower bandgap, which easily leads to the recombination of photogenerated carriers. For MnFe-LDH, its suitable bandgap allows the transition and separation of photogenerated carriers without easy recombination. The photoelectric properties of MnFe-LDH, MnAl-LDH, and ZnFe-LDH were further confirmed by the transient photocurrent response and the EIS Nyquist plots. In Figure S10, MnFe-LDH has the highest

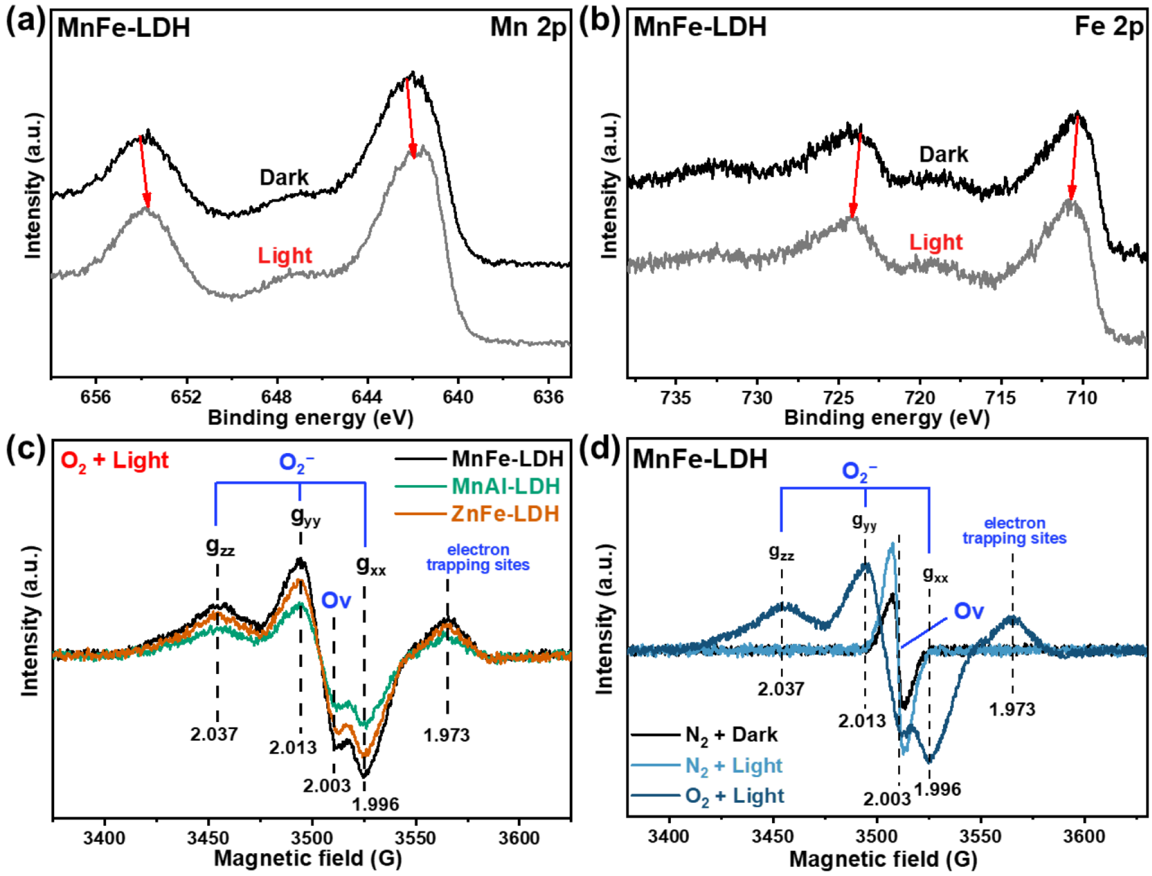

Figure 5. XPS spectra of (a) Mn 2p and (b) Fe 2p for MnFe-LDH under dark and light conditions. (c) *In situ* EPR spectra over MnFe-LDH, MnAl-LDH, and ZnFe-LDH collected in a flow of O_2 under light conditions. (d) *In situ* EPR spectra over MnFe-LDH collected in a flow of N_2 or O_2 under dark or light conditions.

transient photocurrent intensity and the smallest EIS Nyquist radius, indicating that MnFe-LDH has the best photogenerated carrier separation efficiency and the fastest migration rate, resulting from the intensive built-in electric field in the Mn^{2+}—O—Fe^{3+} domain.

The formation of photogenerated electrons and holes in the built-in electric field can promote and participate in the generation of ROS during the reaction.[55−57] *In situ* EPR characterizations under the conditions of light and O_2 are shown in Figure 5c. The signal around $g = 1.973$ is attributed to surface electron trapping sites related to oxygen species, and another set of signals ($g_{xx} = 1.996$, $g_{yy} = 2.013$, $g_{zz} = 2.037$) is attributed to paramagnetic superoxide O_2^- species.[52,58] It is found that the signals for all ROS in MnFe-LDH are stronger than those in ZnFe-LDH and MnAl-LDH. Furthermore, the formation process of ROS is explored in Figure 5d. Specifically, under N_2 and dark conditions, the Ov signals are observed, which are further enhanced once light is introduced, indicating that the lattice oxygen on MnFe-LDH is easily activated to create Ov. Additionally, when the atmosphere is changed from N_2 to O_2, the Ov signals are weakened, while more ROS signals of O_2^- are generated from the O_2 activation in Ov sites.

Therefore, owing to the greater bimetallic asymmetry of the Mn^{2+}—O—Fe^{3+} domain in MnFe-LDH, the elongation of Mn—O bonds and contraction of Fe—O bonds are obviously formed, leading to the activation of lattice oxygen and an intensive built-in electric field, which promote the O_2 adsorbed in the generated Ov for ROS formation under light, resulting in the superior toluene oxidation performance of MnFe-LDH.

3.4. Photocatalytic Mechanism of Toluene Oxidation.

To explore the reaction mechanism of photocatalytic toluene oxidation, the adsorption energies of toluene on MnFe-LDH, MnAl-LDH, and ZnFe-LDH are first investigated through DFT calculations. As shown in Figure 6a, toluene could be adsorbed on all three photocatalysts, and the adsorption capacity follows the order of ZnFe-LDH < MnFe-LDH < MnAl-LDH. Moreover, the *in situ* DRIFTS tests in the dark were carried out on MnFe-LDH, MnAl-LDH, and ZnFe-LDH in order to study the differences in toluene adsorption. In Figure 6b, the peak at around 1660 cm^{-1} attributed to the hydroxyl groups in the LDH samples[23,59] decreases, suggesting that the hydroxyl groups in the photocatalyst act as the adsorption site for toluene, consistent with the calculation models. In addition, a series of characteristic peaks of toluene appear, in which the range of about 1530−1630 cm^{-1} can be attributed to the υ (C═C) of the aromatic ring.[23,60] It is observed that the strongest toluene signal appears on MnAl-LDH, while the weakest one is found on ZnFe-LDH, which is consistent with the adsorption energy results. Generally, the oxygen gas is adsorbed not only on oxygen vacancies but also on hydroxyl groups via hydrogen bonding interactions. Since both toluene and oxygen are reactants, their competitive adsorption on the LDH surface may influence the toluene degradation. It shows that MnAl-LDH exhibits the strongest toluene adsorption, which inhibits oxygen adsorption and ROS generation. In contrast, ZnFe-LDH shows very weak toluene adsorption, leading to a reduced level of activation and conversion of toluene on the surface. MnFe-LDH exhibits

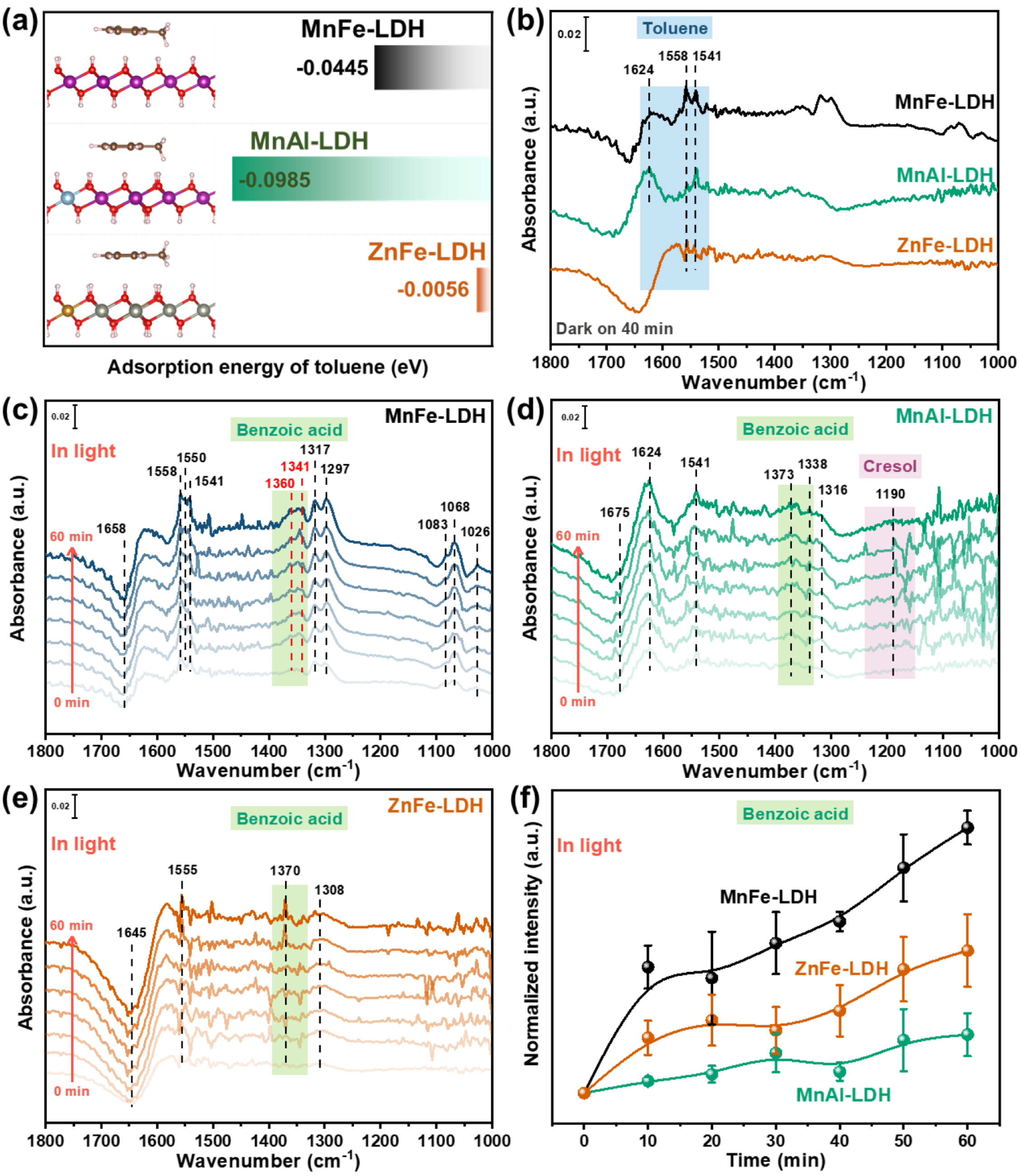

Figure 6. (a) DFT calculations of adsorption energies of toluene on MnFe-LDH, MnAl-LDH, and ZnFe-LDH. *In situ* DRIFTS of toluene and O_2 adsorption (b) in the dark for 40 min, and in light on (c) MnFe-LDH, (d) MnAl-LDH, and (e) ZnFe-LDH. (f) The intensity variation of the benzoic acid intermediate with time in light.

moderate adsorption of toluene, which does not significantly inhibit oxygen adsorption and still allows a sufficient amount of toluene participation in the reaction. This balanced adsorption behavior is one of the important factors enhancing catalytic activity. Therefore, the weakest adsorption of toluene on ZnFe-LDH is unfavorable for the oxidation reaction of toluene on its surface, whereas the excessively strong interaction between the hydroxyl groups (MnAl-LDH) and the benzene ring (toluene) may attack the benzene ring rather than promoting methyl oxidation.

Furthermore, the *in situ* DRIFTS analysis of toluene and O_2 adsorption under light conditions was carried out, as shown in Figure 6c−e. It was observed that the illumination accelerates the oxidation of toluene, with signals of oxidized species detected across all three samples, such as the signals of benzyl alcohol[61] (1026, 1068, and 1083 cm^{-1}), benzaldehyde[62−64] (1297 and 1317 cm^{-1}), and benzoic acid[65,66] (1341 and 1360 cm^{-1}). The signals of oxidized species on MnFe-LDH are more intensive, indicating its stronger oxidation capability for toluene.[19] In the toluene oxidation reaction, the formation of a benzoic acid intermediate is more conducive to further ring opening and mineralization of toluene. Therefore, we analyzed the intensity variation of the benzoic acid intermediate over time under light. In Figure 6f, the results indicate stronger benzoic acid signals on the surface of MnFe-LDH, suggesting that due to its enhanced ability to generate ROS, MnFe-LDH can achieve rapid and deep oxidation of toluene, thereby accelerating its ring-opening mineralization. In contrast, fewer

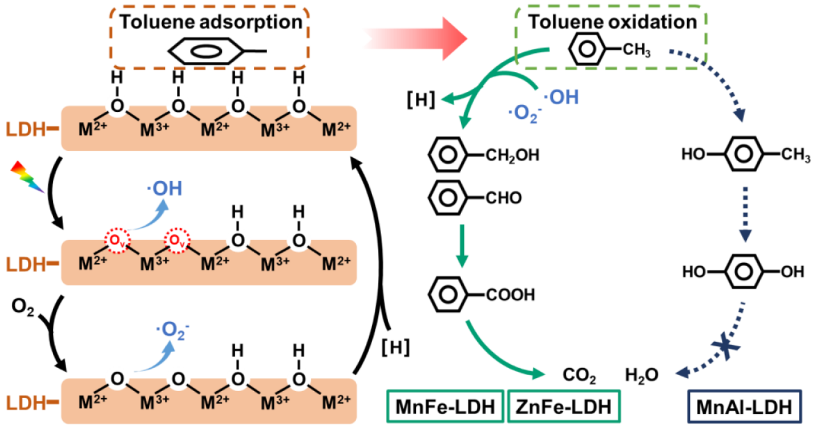

Figure 7. Proposed mechanism for the photocatalytic oxidation of toluene on the LDHs.

benzoic acid signals are observed on the surface of ZnFe-LDH which is attributed to its weaker adsorption capacity for toluene, resulting in lower oxidation activity. Additionally, on the surface of MnAl-LDH, the benzoic acid signal is the weakest, while cresol intermediate is observed, combined with its stronger adsorption interaction of the aromatic ring of toluene, which suggests that excessively strong adsorption of the aromatic ring on MnAl-LDH inhibits methyl oxidation and ring opening, while the generated cresol intermediates subsequently transform into hydroquinone intermediates, which disfavor the ring opening and mineralization of toluene.

In summary, the oxidation process of toluene on MnFe-LDH mainly includes the following steps (Figure 7): (1) The toluene is adsorbed onto the catalyst through interactions with abundant hydroxyl groups on the MnFe-LDH surface. (2) Under illumination, the lattice oxygen of MnFe-LDH is further activated, along with the photogenerated carriers to generate hydroxyl radicals (•OH) and O_V. Additionally, the O_2 adsorbed on the formed O_V can be converted into O_2^- and other ROS. (3) Under the attack of these ROS, the adsorbed toluene is oxidized into benzyl alcohol, benzaldehyde, and benzoic acid and undergoes rapid ring-opening reactions to convert into CO_2 and H_2O. For ZnFe-LDH, its weak adsorption of toluene makes it difficult to activate and oxidize toluene, leading to a poorer performance. For MnAl-LDH, the strong adsorption interaction of the aromatic ring of toluene inhibits methyl oxidation and ring opening, and the fewer generated ROS make it difficult to oxidize hydroquinone intermediates and achieve toluene mineralization. Due to the synergistic activation of the aromatic ring and methyl group of toluene, as well as the greater formation of ROS from better lattice oxygen activation of the bimetallic asymmetry, MnFe-LDH exhibits superior toluene oxidation performance compared to MnAl-LDH and ZnFe-LDH.

4. CONCLUSIONS

In this work, the LDH photocatalysts with different bimetallic asymmetry and metal−oxygen bonds are designed for photocatalytic toluene oxidation. The MnFe-LDH photocatalyst exhibits the best toluene oxidation performance due to its significant elongated Mn−O bonds and contracted Fe−O bonds, leading to the lattice oxygen activation and built-in electric field in light for ROS, which achieves deep oxidation of the adsorbed toluene.

■ ASSOCIATED CONTENT

SI Supporting Information

The Supporting Information is available free of charge at https://pubs.acs.org/doi/10.1021/acs.inorgchem.5c02813.

Details of characterizations and results of XRD, FT-IR spectra, UV−vis DRS, photocatalytic toluene oxidation performance, XPS spectra, transient photocurrent response, and EIS (PDF)

■ AUTHOR INFORMATION

Corresponding Authors

Weixin Zou − *State Key Laboratory of Water Pollution Control and Green Resource Recycling, School of Environment, Key Laboratory of Mesoscopic Chemistry of MOE, Institute of Theoretical and Computational Chemistry, School of Chemistry and Chemical Engineering, Jiangsu Key Laboratory of Vehicle Emissions Control, Nanjing University, Nanjing 210093, P. R. China;* orcid.org/0000-0001-5001-2841; Email: wxzou2016@nju.edu.cn

Tao Liu − *State Key Laboratory of Water Pollution Control and Green Resource Recycling, School of Environment, Key Laboratory of Mesoscopic Chemistry of MOE, Institute of Theoretical and Computational Chemistry, School of Chemistry and Chemical Engineering, Jiangsu Key Laboratory of Vehicle Emissions Control, Nanjing University, Nanjing 210093, P. R. China; School of Environmental Engineering, Nanjing Institute of Technology, Nanjing 211167, P.R. China;* Email: liut@njit.edu.cn

Authors

Haohong Liao − *State Key Laboratory of Water Pollution Control and Green Resource Recycling, School of Environment, Key Laboratory of Mesoscopic Chemistry of MOE, Institute of Theoretical and Computational Chemistry, School of Chemistry and Chemical Engineering, Jiangsu Key Laboratory of Vehicle Emissions Control, Nanjing University, Nanjing 210093, P. R. China*

Jingfang Sun − *Centre for Shared Scientific Research Facilities, Nanjing University, Nanjing 210093, P. R. China;* orcid.org/0000-0003-1963-4874

Xiuwen Wang − *Center for Microscopy and Analysis, Nanjing University of Aeronautics and Astronautics, Nanjing 211106, P. R. China*

Qing Tong − *Centre for Shared Scientific Research Facilities, Nanjing University, Nanjing 210093, P. R. China*

Lin Dong − *State Key Laboratory of Water Pollution Control and Green Resource Recycling, School of Environment, Key Laboratory of Mesoscopic Chemistry of MOE, Institute of Theoretical and Computational Chemistry, School of Chemistry and Chemical Engineering, Jiangsu Key Laboratory of Vehicle Emissions Control, Nanjing University, Nanjing 210093, P. R. China;* orcid.org/0000-0002-8393-6669

Complete contact information is available at: https://pubs.acs.org/10.1021/acs.inorgchem.5c02813

Author Contributions

[#]H.L. and J.S. contributed equally to this work.

Notes

The authors declare no competing financial interest.

■ ACKNOWLEDGMENTS

This work was supported by the National Natural Science Foundation of China (62375120, 22476085, and 22106067) and the Natural Science Foundation of Jiangsu Province of China (BK20240171 and BK20231513).

■ REFERENCES

(1) He, C.; Cheng, J.; Zhang, X.; Douthwaite, M.; Pattisson, S.; Hao, Z. Recent advances in the catalytic oxidation of volatile organic compounds: A review based on pollutant sorts and sources. *Chem. Rev.* **2019**, *119*, 4471−4568.

(2) Lewis, A. C.; Jenkins, D.; Whitty, C. J. M. Hidden harms of indoor air pollution - five steps to expose them. *Nature* **2023**, *614*, 220−223.

(3) Sethi, S.; Nanda, R.; Chakraborty, T. Clinical application of volatile organic compound analysis for detecting infectious diseases. *Clin. Microbiol. Rev.* **2013**, *26*, 462−475.

(4) Taufik, A.; Yoko, A.; Han, C.; Wahyudiono; Ohara, S.; Adschiri, T. Facet dependent Pt adsorption on rutile TiO_2 surface for efficient photocatalytic VOCs removal. *Small* **2025**, *21* (15), 2412727.

(5) Yang, D.; Guo, Y.; Yu, Z.; Jiang, Z.; Xiang, W.; Wu, X.; Wang, J. Surface oxygen vacancy engineering for enhanced volatile organic compounds removal in solar-interfacial water evaporation. *Environ. Sci. Technol.* **2025**, *59*, 7117−7128.

(6) Ye, S.; Ban, T.; Zhang, Z.; Liu, B.; Xie, R.; Ye, X.; Zhong, Y.; Cao, J.; Huang, L.; Huang, H. Exceptional resistance to chlorine-induced photocatalytic poisoning via vacuum UV irradiation. *Environ. Sci. Technol.* **2025**, *59*, 5796−5807.

(7) Wang, J.; Yang, C.; Ye, D.; Hu, Y. The mechanism of effective photocatalytic degradation of toluene by Zr/Ti bimetallic metal-organic framework derivatives loaded with TiO_2. *Appl. Catal., B* **2025**, *361*, 124635.

(8) Li, Y.; Chen, B.; Liu, L.; Zhu, B.; Zhang, D. Water-resistance-based S-scheme heterojunction for deep mineralization of toluene. *Angew. Chem., Int. Ed.* **2024**, *63* (11), No. e202319432.

(9) Ma, H.; Hu, X.; Wang, X.; Xu, W.; Shen, Y.; Fang, R.; Li, Y.; Liu, Y.; Dong, F. D-band center modulated water molecule adsorption and activation towards highly photocatalytic toluene mineralization. *Appl. Catal., B* **2025**, *361*, 124638.

(10) Li, X.; Zhang, L.; Yang, Z.; Wang, P.; Yan, Y.; Ran, J. Adsorption materials for volatile organic compounds (VOCs) and the key factors for VOCs adsorption process: A review. *Sep. Purif. Technol.* **2020**, *235*, 116213.

(11) Shen, Y.; Deng, J.; Hu, X.; Chen, X.; Yang, H.; Cheng, D.; Zhang, D. Expediting toluene combustion by harmonizing the Ce−O strength over Co-doped CeZr oxide catalysts. *Environ. Sci. Technol.* **2023**, *57*, 1797−1806.

(12) Liu, B.; Hu, Z.; Zhang, B.; Liu, B.; Li, G.; Zhang, T.; Ji, J.; Li, K.; Dai, W.; Zhang, J.; Huang, H. Deep photocatalytic oxidation of aromatic VOCs on ZnSn LDH: Promoting role of electron enrichment of surface hydroxyl. *ACS Catal.* **2023**, *13*, 7857−7867.

(13) Zhang, Y.; Wang, Y.; Xie, R.; Huang, H.; Leung, M. K. H.; Li, J.; Leung, D. Y. C. Photocatalytic oxidation for volatile organic compounds elimination: From fundamental research to practical applications. *Environ. Sci. Technol.* **2022**, *56*, 16582−16601.

(14) Yu, P.; Li, N.; Zou, W.; Wei, X.; Ji, J.; Han, L.; Cai, Y.; Tan, W.; Gao, B.; Dong, L. K^+ and CeO_2 nanoparticles modified OMS-2 nanorods for enhanced activity and stability of photocatalytic toluene oxidation: K^+ charge modulation and mechanistic investigation. *Chem. Eng. J.* **2023**, *451*, 138943.

(15) Shayegan, Z.; Lee, C.-S.; Haghighat, F. TiO_2 photocatalyst for removal of volatile organic compounds in gas phase-A review. *Chem. Eng. J.* **2018**, *334*, 2408−2439.

(16) El Khawaja, R.; Rochard, G.; Genty, E.; Poupin, C.; Siffert, S.; Cousin, R. Optimization of Mn-Mg-Al mixed oxides composition on their activity towards the total oxidation of aromatic and oxygenated VOCs. *Eur. J. Inorg. Chem.* **2023**, *26* (20), No. e202300213.

(17) Fu, X.; Wang, J.; Huang, D.; Meng, S.; Zhang, Z.; Li, L.; Miao, T.; Chen, S. Trace amount of SnO_2-decorated $ZnSn(OH)_6$ as highly efficient photocatalyst for decomposition of gaseous benzene: Synthesis, photocatalytic activity, and the unrevealed synergistic effect between $ZnSn(OH)_6$ and SnO_2. *ACS Catal.* **2016**, *6*, 957−968.

(18) Chen, J.; He, Z.; Ji, Y.; Li, G.; An, T.; Choi, W. ·OH radicals determined photocatalytic degradation mechanisms of gaseous styrene in TiO_2 system under 254 nm versus 185 nm irradiation: Combined experimental and theoretical studies. *Appl. Catal., B* **2019**, *257*, 117912.

(19) Liu, B.; Zhang, B.; Ji, J.; Li, K.; Cao, J.; Feng, Q.; Huang, H. Effective regulation of surface bridging hydroxyls on TiO_2 for superior photocatalytic activity via ozone treatment. *Appl. Catal., B* **2022**, *304*, 120952.

(20) Liu, Y.; Chen, S.; Li, K.; Wang, J.; Chen, P.; Wang, H.; Li, J.; Dong, F. Promote the activation and ring opening of intermediates for stable photocatalytic toluene degradation over Zn-Ti-LDH. *J. Colloid Interface Sci.* **2022**, *606*, 1435−1444.

(21) Zhang, J.; Shen, B.; Hu, Z.; Zhen, M.; Guo, S.-Q.; Dong, F. Uncovering the synergy between Mn substitution and O vacancy in ZnAl-LDH photocatalyst for efficient toluene removal. *Appl. Catal., B* **2021**, *296*, 120376.

(22) Dong, X.; Cui, Z.; Sun, Y.; Dong, F. Humidity-independent photocatalytic toluene mineralization benefits from the utilization of edge hydroxyls in layered double hydroxides (LDHs): A combined operando and theoretical investigation. *ACS Catal.* **2021**, *11*, 8132−8139.

(23) Liu, B.; Zhang, B.; Liu, B.; Hu, Z.; Dai, W.; Zhang, J.; Feng, F.; Lan, B.; Zhang, T.; Huang, H. Surface hydroxyl and oxygen vacancies engineering in ZnSnAl LDH: Synergistic promotion of photocatalytic oxidation of aromatic VOCs. *Environ. Sci. Technol.* **2024**, *58*, 4404−4414.

(24) Chen, L.; Chen, P.; Wang, H.; Cui, W.; Sheng, J.; Li, J.; Zhang, Y.; Zhou, Y.; Dong, F. Surface lattice oxygen activation on $Sr_2Sb_2O_7$ enhances the photocatalytic mineralization of toluene: From reactant activation, intermediate conversion to product desorption. *ACS Appl. Mater. Interfaces* **2021**, *13*, 5153−5164.

(25) Wang, J.; Zhang, M.; Yang, G.; Song, W.; Zhong, W.; Wang, X.; Wang, M.; Sun, T.; Tang, Y. Heterogeneous bimetallic Mo-NiP_x/NiS_y as a highly efficient electrocatalyst for robust overall water splitting. *Adv. Funct. Mater.* **2021**, *31* (33), 2101532.

(26) Wang, M.; Zhang, M.; Song, W.; Zhou, L.; Wang, X.; Tang, Y. Heteroatom-doped amorphous cobalt-molybdenum oxides as a promising catalyst for robust hydrogen evolution. *Inorg. Chem.* **2022**, *61*, 5033−5039.

(27) Zhu, D.; Huang, Y.; Li, R.; Peng, S.; Wang, P.; Cao, J. Constructing active Cu^{2+}-O-Fe^{3+} sites at the CuO-Fe_3O_4 interface to promote activation of surface lattice oxygen. *Environ. Sci. Technol.* **2023**, *57*, 17598−17609.

(28) Shen, Y.; Deng, J.; Han, L.; Ren, W.; Zhang, D. Low-temperature combustion of toluene over Cu-doped $SmMn_2O_5$ mullite

catalysts via creating highly active Cu^{2+}-O-Mn^{4+} sites. *Environ. Sci. Technol.* **2022**, *56*, 10433−10441.

(29) Hong, X.; Zhu, S.; Xia, M.; Du, P.; Wang, F. Investigation of the efficient adsorption performance and adsorption mechanism of 3D composite structure La nanosphere-coated Mn/Fe layered double hydrotalcite on phosphate. *J. Colloid Interface Sci.* **2022**, *614*, 478−488.

(30) Kresse, G.; Furthmüller, J. Efficiency of Ab-Initio total energy calculations for metals and semiconductors using a plane-wave basis set. *Comput. Mater. Sci.* **1996**, *6*, 15−50.

(31) Kresse, G.; Furthmüller, J. Efficient iterative schemes for Ab initio total-energy calculations using a plane-wave basis set. *Phys. Rev. B* **1996**, *54*, 11169−11186.

(32) Perdew, J. P.; Burke, K.; Ernzerhof, M. Generalized gradient approximation made simple. *Phys. Rev. Lett.* **1996**, *77*, 3865−3868.

(33) Kresse, G.; Joubert, D. From ultrasoft pseudopotentials to the projector augmented-wave method. *Phys. Rev. B* **1999**, *59*, 1758−1775.

(34) Blöchl, P. E. Projector augmented-wave method. *Phys. Rev. B* **1994**, *50*, 17953−17979.

(35) Grimme, S.; Antony, J.; Ehrlich, S.; Krieg, H. A consistent and accurate ab initio parametrization of density functional dispersion correction (DFT-D) for the 94 elements H-Pu. *J. Chem. Phys.* **2010**, *132* (15), 154104.

(36) Bader, R. F. W. A quantum theory of molecular structure and its applications. *Chem. Rev.* **1991**, *91*, 893−928.

(37) Henkelman, G.; Arnaldsson, A.; Jónsson, H. A fast and robust algorithm for Bader decomposition of charge density. *Comput. Mater. Sci.* **2006**, *36*, 354−360.

(38) Mo, J.; Zhang, Y.; Xu, Q. Effect of water vapor on the by-products and decomposition rate of ppb-level toluene by photocatalytic oxidation. *Appl. Catal., B* **2013**, *132−133*, 212−218.

(39) Zhao, W.; Dai, J.; Liu, F.; Bao, J.; Wang, Y.; Yang, Y.; Yang, Y.; Zhao, D. Photocatalytic oxidation of indoor toluene: Process risk analysis and influence of relative humidity, photocatalysts, and VUV irradiation. *Sci. Total Environ.* **2012**, *438*, 201−209.

(40) You, J.-W.; Vikrant, K.; Lim, D.-H.; Verma, S.; Kukkar, D.; Anwer, H.; Kim, K.-H. Photocatalytic potential of a titanium dioxide-supported platinum catalyst against VOCs with complicated composition under varying humidity conditions. *J. Cleaner Prod.* **2022**, *371*, 133487.

(41) Zhong, L.; Brancho, J. J.; Batterman, S.; Bartlett, B. M.; Godwin, C. Experimental and modeling study of visible light responsive photocatalytic oxidation (PCO) materials for toluene degradation. *Appl. Catal., B* **2017**, *216*, 122−132.

(42) Ly, H. N.; Parasuraman, V.; Lee, H.; Sheraz, M.; Anus, A.; Lee, W. R.; Kim, S. Enhancing air treatment through controlled fabrication of transition metal-doped titanium dioxide nanocomposites for photocatalytic toluene degradation. *Chemosphere* **2024**, *351*, 141261.

(43) Bo, L.; Xie, S.; Meng, H.; Liu, J.; Gao, B. Photocatalytic oxidation of gaseous toluene by visible-light-driven $CoCuMnO_x$: Performance and mechanism. *Catal. Lett.* **2017**, *147*, 1623−1630.

(44) Xiao, M.; Yu, X.; Guo, Y.; Ge, M. Boosting toluene combustion by tuning electronic metal-support interactions in *in situ* grown Pt@Co_3O_4 catalysts. *Environ. Sci. Technol.* **2022**, *56*, 1376−1385.

(45) Wang, B.; Zhuo, Z.; Li, H.; Liu, S.; Zhao, S.; Zhang, X.; Liu, J.; Xiao, D.; Yang, W.; Yu, H. Stacking faults inducing oxygen anion activities in Li_2MnO_3. *Adv. Mater.* **2023**, *35* (22), 2207904.

(46) Liu, W.; Bai, P.; Wei, S.; Yang, C.; Xu, L. Gadolinium changes the local electron densities of nickel 3d orbitals for efficient electrocatalytic CO_2 reduction. *Angew. Chem., Int. Ed.* **2022**, *61* (18), No. e202201166.

(47) Liu, X.; Mi, J.; Shi, L.; Liu, H.; Liu, J.; Ding, Y.; Shi, J.; He, M.; Wang, Z.; Xiong, S.; Zhang, Q.; Liu, Y.; Wu, Z. S.; Chen, J.; Li, J. *In situ* modulation of a-site vacancies in $LaMnO_{3.15}$ perovskite for surface lattice oxygen activation and boosted redox reactions. *Angew. Chem., Int. Ed.* **2021**, *60*, 26747−26754.

(48) Liu, M.; Liu, Y.; Zhang, X.; Li, L.; Xue, X.; Humayun, M.; Yang, H.; Sun, L.; Bououdina, M.; Zeng, J.; et al. Altering the symmetry of Fe-N-C by axial Cl-mediation for high-performance zinc-air batteries. *Angew. Chem., Int. Ed.* **2025**, *64*, No. e202504923.

(49) Li, S.; Zhou, W.; Liu, F.; Guan, C.; Gao, X.; Zhang, Y.; Jin, R.; Lai, Y.; Zhang, Z. Mitigating long range Jahn-Teller ordering to stabilize Mn redox reaction in biphasic layered sodium oxide. *Adv. Energy Mater.* **2025**, *15* (10), 2403955.

(50) Zhang, X.; Tang, J.; Wang, L.; Wang, C.; Chen, L.; Chen, X.; Qian, J.; Pan, B. Nanoconfinement-triggered oligomerization pathway for efficient removal of phenolic pollutants via a Fenton-like reaction. *Nat. Commun.* **2024**, *15* (1), 917.

(51) Wang, J.; Li, J.; Jiang, C.; Zhou, P.; Zhang, P.; Yu, J. The effect of manganese vacancy in birnessite-type MnO_2 on room-temperature oxidation of formaldehyde in air. *Appl. Catal., B* **2017**, *204*, 147−155.

(52) An, D.; Yang, S.; Cheng, Q.; Yan, W.; Sun, J.; Zou, W.; Sun, C.; Tang, C.; Dong, L. Water-driven surface lattice oxygen activation in MnO_2 for promoted low-temperature NH_3-SCR. *Environ. Sci. Technol.* **2024**, *58*, 16974−16983.

(53) Liu, Z.; Liang, J.; Song, Q.; Li, Y.; Zhang, Z.; Zhou, M.; Wei, W.; Xu, H.; Lee, C.-S.; Li, H.; Jiang, Z. Construction atomic-level N-P charge transfer channel for boosted CO_2 photoreduction. *Appl. Catal., B* **2023**, *328*, 122472.

(54) Ran, J.; Chen, L.; Wang, D.; Talebian-Kiakalaieh, A.; Jiao, Y.; Adel Hamza, M.; Qu, Y.; Jing, L.; Davey, K.; Qiao, S.-Z. Atomic-level regulated 2D $ReSe_2$: A universal platform boostin photocatalysis. *Adv. Mater.* **2023**, *35* (19), 2210164.

(55) Zhou, X.; Wang, T.; He, D.; Chen, P.; Liu, H.; Lv, H.; Wu, H.; Su, D.; Pang, H.; Wang, C. Efficient photocatalytic desulfurization in air through improved photogenerated carriers separation in MOF MIL101/carbon dots-g-C_3N_4 nanocomposites. *Angew. Chem., Int. Ed.* **2024**, *63* (35), No. e202408989.

(56) Zhao, W.; Kan, L.; Wang, D.; Zhai, L.; Li, X.; Zhou, S.; Liu, G.; Zhu, L.; Gu, P. Coupling ionic polarization, electron sponge effect by one-pot hypercrosslinking, pyridiniumnation of photosensitizer-based porous organic polymers for enhancing advanced oxidation process. *Adv. Funct. Mater.* **2025**, 2425137.

(57) Wang, Y.; Cai, C. Photocatalytic oxidation of 5-hydroxymethylfurfural to selective products by noble metal-free Z-scheme heterostructures α-Fe_2O_3/$Zn_{0.5}Cd_{0.5}S$. *ACS Catal.* **2025**, *15*, 3451−3463.

(58) Yu, X.; Dai, L.; Deng, J.; Liu, Y.; Jing, L.; Zhang, X.; Gao, R.; Hou, Z.; Wei, L.; Dai, H. An isotopic strategy to investigate the role of water vapor in the oxidation of 1,2-dichloroethane over the Ru/WO_3 or Ru/TiO_2 catalyst. *Appl. Catal., B* **2022**, *305*, 121037.

(59) Shivaraju, H. P.; Ashika, O. N.; Harini, R.; Yashas, S. R.; Maleki, A.; Shahmoradi, B.; Yetilmezsoy, K.; Kitirote, W. Facile synthesis and characterization of $Zn_5(OH)_8Cl_2{\cdot}H_2O$ nanostructure for the bio-methanation process. *Mater. Lett.* **2021**, *282*, 128808.

(60) Mamaghani, A. H.; Haghighat, F.; Lee, C.-S. Gas phase adsorption of volatile organic compounds onto titanium dioxide photocatalysts. *Chem. Eng. J.* **2018**, *337*, 60−73.

(61) Zhao, C.; Hao, Q.; Zhang, Q.; Yan, N.; Liu, J.; Dou, B.; Bin, F. Catalytic self-sustained combustion of toluene and reaction pathway over $Cu_xMn_{1-x}Ce_{0.75}Zr_{0.25}/TiO_2$ catalysts. *Appl. Catal., A* **2019**, *569*, 66−74.

(62) Deveau, P. A.; Arsac, F.; Thivel, P. X.; Ferronato, C.; Delpech, F.; Chovelon, J. M.; Kaluzny, P.; Monnet, C. Different methods in TiO_2 photodegradation mechanism studies: Gaseous and TiO_2-adsorbed phases. *J. Hazard. Mater.* **2007**, *144*, 692−697.

(63) Clawin, P. M.; Friend, C. M.; Al-Shamery, K. Defects in surface chemistry−Reductive coupling of benzaldehyde on rutile TiO_2(110). *Chem.−Eur. J* **2014**, *20*, 7665−7669.

(64) Zhang, M.; Cai, S.; Li, J.; Elimian, E. A.; Chen, J.; Jia, H. Ternary multifunctional catalysts of polymeric carbon nitride coupled with Pt-embedded transition metal oxide to enhance light-driven photothermal catalytic degradation of VOCs. *J. Hazard. Mater.* **2021**, *412*, 125266.

(65) Buchholz, M.; Xu, M.; Noei, H.; Weidler, P.; Nefedov, A.; Fink, K.; Wang, Y.; Wöll, C. Interaction of carboxylic acids with rutile

TiO_2(110): IR-investigations of terephthalic and benzoic acid adsorbed on a single crystal substrate. *Surf. Sci.* **2016**, *643*, 117–123.

(66) Cao, L.; Gao, Z.; Suib, S. L.; Obee, T. N.; Hay, S. O.; Freihaut, J. D. Photocatalytic oxidation of toluene on nanoscale TiO_2 catalysts: Studies of deactivation and regeneration. *J. Catal.* **2000**, *196*, 253–261.

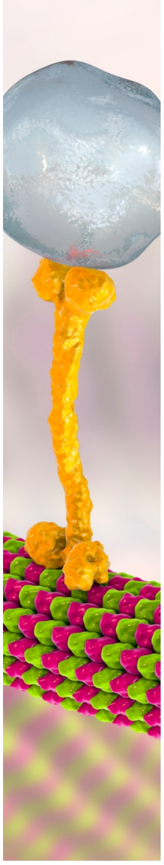

CAS BIOFINDER DISCOVERY PLATFORM™

BRIDGE BIOLOGY AND CHEMISTRY FOR FASTER ANSWERS

Analyze target relationships, compound effects, and disease pathways

Explore the platform

CAS
A division of the American Chemical Society